

Diocotron and Kelvin Mode Damping from a Flux through the Critical Layer

A. A. Kabantsev, C. Y. Chim, T. M. O’Neil, and C. F. Driscoll

Department of Physics, University of California at San Diego, La Jolla, California 92093, USA

(Received 27 August 2013; published 19 March 2014)

Experiments and theory characterize a novel type of spatial Landau damping, caused by a flux of particles through the wave or rotation resonance (critical) layer. Pure electron plasma experiments demonstrate that a steady flux of particles causes *algebraic* damping of diocotron mode amplitudes for azimuthal modes $m = 1$ and $m = 2$, and a simple model of dynamics in the nonlinear cat’s eye clarifies the observations. This flux-driven algebraic damping is related to, but distinct from, the *exponential* decay characteristic of Landau damping. This flux-driven damping applies also to Kelvin waves on 2D vortices, and so may be broadly relevant to plasmas and geophysical flows.

DOI: 10.1103/PhysRevLett.112.115003

PACS numbers: 52.27.Jt, 47.32.C-, 52.35.Kt, 52.35.We

Diocotron modes with azimuthal mode numbers $m = 1, 2, \dots$ are dominant features in the dynamics of non-neutral plasmas in cylindrical [1–10] and toroidal [11] magnetic traps. Moreover, diocotron modes are directly analogous to Kelvin waves on fluid vortices, since the (r, θ) flow of the plasma approximates an inviscid, incompressible column of fluid vorticity [1,2]. In the $m = 1$ diocotron mode, the entire plasma column $E \times B$ drifts around the trap axis due to image charges on the wall, and this corresponds to a vortex “walking” along a wall. This fundamental dynamical motion [3] can be autoresonantly controlled [4], and is now used for “parking” antimatter at desired locations [5,12]. The $m = 2$ diocotron mode [2,6,13] is an elliptical distortion of the charge column, corresponding to a Kelvin wave on a vortex [14].

Spatial Landau damping (or instability) is the idealized resonant interaction between a mode at frequency f_m and the equilibrium plasma rotation $f_E(r)$, at the critical radius R_{cm} where $f_m = mf_E(R_{cm})$ [1,13–16]; this is mathematically analogous to velocity-space Landau damping at velocity v given by $\omega_k = kv$ [1,17]. This inviscid resonance causes exponential mode damping or exponential mode growth, depending on the magnitude and slope of the initial density (or vorticity) at R_{cm} . The exponential growth is commonly observed in hollow beams and plasmas [1,2], and the analogous Kelvin-Helmholtz shear-flow instability is ubiquitous in fluids.

Exponential Landau damping is widely observed in plasmas [1,6,13,15] and geophysical flows [14,18,19]. The early-time reversibility of inviscid Landau damping is demonstrated by observation of “fluid echoes” [20], but the time asymptotics of the Cauchy initial-value problem involves subtle mathematical questions [13,14,16,21]. For moderate initial wave amplitudes, damping typically ceases when the density at the critical layer is trapped in a nonlinear “cat’s eye” flow structure [6,13], and these time-invariant multipole states have been constructed for a variety of geophysical models [22]. Large amplitude

excitation commonly extends the core density into the critical layer, making the damping process visible as spiral arms, and nonlinear interactions at the *beat-wave* critical layer may cause rapid energy transfer between two modes in astrophysical [7] and geophysical [18] flows.

Weak nonideal processes may also cause exponential damping. In plasmas, damping has been observed from rotational pumping of bulk viscosity [9,11] and from z -velocity dissipation on a separatrix [23]. In fluids, viscosity causes spreading of vorticity through critical layers, often combined with other effects [24].

Here, we demonstrate that a weak nonideal “mobility” flux of particles outward through the critical layer causes strong *algebraic* damping of diocotron modes, completely symmetrizing the plasma. This is the first demonstration of a new aspect of wave-fluid interactions at the critical layer, broadly relevant to plasmas and geophysical flows. We also present a sketch of nascent theory which characterizes the fundamentals of the process.

We find that the weak outward flux changes the temporal character of the damping, since it is now a *driven* evolution. Landau damping describes filamentation and phase mixing of the *initial* density, with resulting outward transport of particles. In contrast, the novel flux-driven damping is determined by the *present* magnitudes of the wave and outward flux.

Experimentally, the nonideal outward flux is caused by trap θ asymmetries, and can be controlled in magnitude. The flux has no significant effect on the mode until the flux reaches the critical radius, at which time strong damping begins. Since weak nonideal particle fluxes are endemic to plasma traps, but are difficult to detect or control, this flux-driven damping may occur commonly. Also, it is generally presumed that Landau damping is zero for the $m = 1$ mode because the critical radius is at the wall where the density is zero, but here, the commonly observed radial particle loss is shown to cause unexpected $m = 1$ mode damping.

The experiments are performed on quiescent, pure electron plasma columns, where the (r, θ) drift dynamics approximates an incompressible fluid [2,11], with electron-electron collisions causing “viscous” relaxation [25] corresponding to a fluid Reynolds number $\text{Re} \sim 10^5$. The electrons are confined radially by a uniform magnetic field $B = 12 \text{ kG } \hat{z}$, and are confined axially by negative voltages on the ends of the cylindrical wall ($R_w = 35 \text{ mm}$), with axial column length $L_p \sim 48 \text{ cm}$. Axial variations are averaged out by rapid bouncing of individual electrons ($T \sim 0.05 \rightarrow 0.5 \text{ eV}$ in the core and halo), and the (r, θ) evolution is predominantly determined by the drift-Poisson equations [1,2]. The electron column has monotonically decreasing density profile $n(r)$, with total line density $N_L(R_w) \equiv \int r dr d\theta n(r, \theta) \sim 6 \times 10^7 \text{ cm}^{-1}$, and Poisson’s equation then gives a monotonically decreasing $E \times B$ drift rotation profile $f_E(r) = (c/2\pi Br)\partial\phi/\partial r$.

The z -averaged electron density $n(r, \theta, t)$ is measured (destructively) by dumping the plasma onto a phosphor screen, giving images such as Fig. 1. Here, an $m = 2$ mode on the central plasma is being damped by density transported out past the critical radius. The θ -averaged profiles of $f_E(r)$ and $n(r; t)$ at 7 times are shown in Fig. 2(a).

The weak outward particle flux is generated by θ -asymmetric fields applied to the trap, which exert a weak drag on the rotating plasma. We apply a magnetic tilt of angle ϵ_B [milliradians] or a z -localized quadrupole wall voltage ϵ_V [Volts], or both. This results in a diffuse “halo” of electrons ($n_h \gtrsim 10^5 \text{ cm}^{-3}$) expanding outward with velocity $v_h \gtrsim 0.2 \text{ mm/s}$, giving flux $F = n_h v_h \gtrsim 2 \times 10^3 / \text{cm}^2 \text{ s}$.

The small-amplitude diocotron modes are surface waves, corresponding to Kelvin waves on the surface of a vortex.

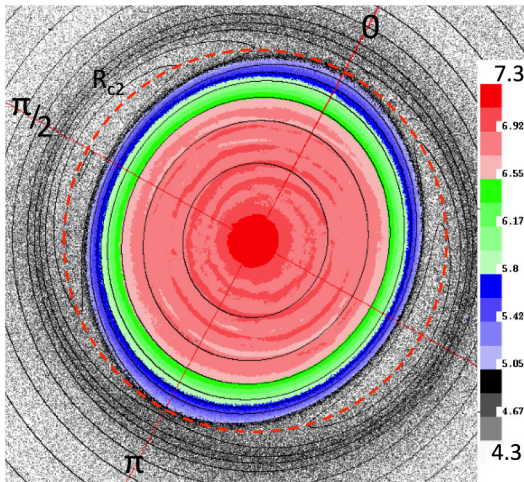


FIG. 1 (color online). Camera image of $n(r, \theta)$ at 25 sec, showing elliptical wave amplitude $D_2 = 0.4 \text{ mm}$ after excitation to $D_2 \sim 0.8 \text{ mm}$ at $t = 0$. Superimposed contours show calculated wave-frame potential (stream function) $\Phi(r, \theta)$ with “cat’s eye” trapping regions.

For a “top-hat” density profile of radius R_p , the plasma edge would be at $R_p + D_m \cos(m\theta - 2\pi f_m t)$, with mode frequency $f_m = f_E[(m-1) + (R_p/R_w)^{2m}]$. At large amplitudes, the low-frequency $m = 1$ mode is better described as a center-of-mass displacement orbiting the trap center [3]. For the nonuniform $n(r)$ of Figs. 1 and 2, we calculate the mean square radius $\langle r^2 \rangle^{1/2}$, giving $R_p \equiv \sqrt{2\langle r^2 \rangle^{1/2}} = 13.4 \text{ mm}$, and the wave quadrupole moment is $q_2 = \langle r^2 \cos(2\theta) \rangle / \langle r^2 \rangle = 0.064$, giving effective edge displacement $D_2 \equiv q_2 R_p / 2 = 0.43 \text{ mm}$. The time evolution of these wave amplitudes $D_m(t)$ is obtained non-destructively from digitized wall signals, calibrated by the image analysis.

The outward flux of particles causes strong diocotron mode damping when the particles reach the wave or rotation critical layer at R_{c2} . Figure 3 shows time evolutions of the $m = 2$ wave amplitude $d_2 \equiv D_2/R_p$, for various fluxes controlled by ϵ_B . The waves are nominally stable, with the visible 10% growth over the first 10 sec caused by effective wall resistance in the amplifier circuits. Beginning at time t_* when the halo flux reaches $R_{c2} = 19 \text{ mm}$, there is strong algebraic damping, as

$$d_2(t) = d_2(t_*) - \gamma_2(t - t_*), \quad (1)$$

with γ_2 larger when the outward flux is made larger.

For the $\epsilon_B = 0$ case the halo flux reaches R_{c2} at $t_* \approx 20 \text{ sec}$. Figure 2(b) shows the corresponding θ -averaged $n(r, t)$ at $t = 20$ and 35, with and without the launched wave. These radial profiles clearly show the wave transporting density across the resonant structure, with consequent damping of the wave itself.

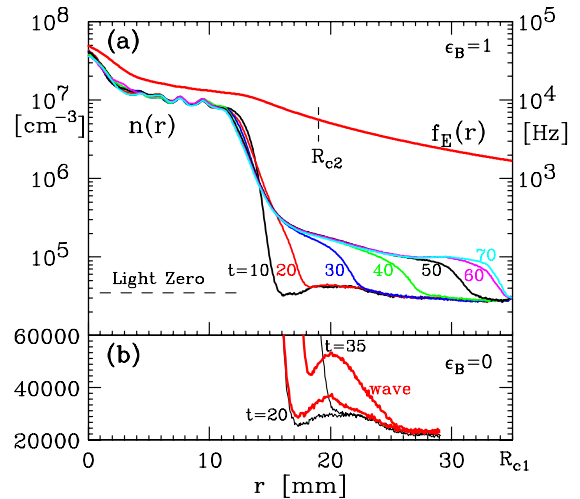


FIG. 2 (color online). (a) Measured θ -averaged electron density (vorticity) $n(r)$ and calculated rotation frequency $f_E(r)$ at times 10 \rightarrow 70 sec, showing a weak “halo” flux propagating outward. (b) Measured density near the wave-fluid resonance layer R_{c2} at $t = 20$ and 35, with and without wave excitation.

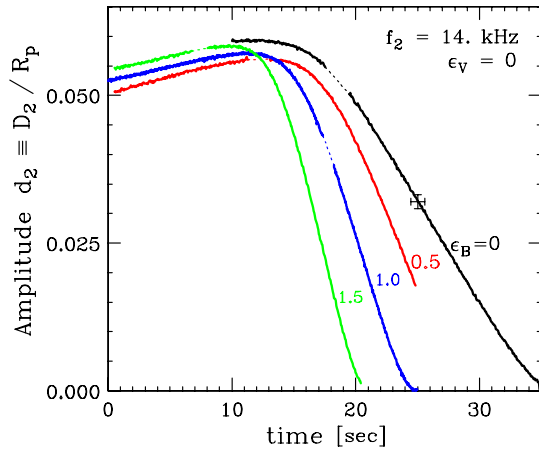


FIG. 3 (color online). Time evolutions of wave amplitude $d_2(t)$ with 4 levels of asymmetry-induced halo flux, showing algebraic damping after the flux reaches the critical radius r_2 . The cross corresponds to Fig. 1.

Similarly, the $m = 1$ diocotron mode shows algebraic damping after the halo flux reaches the resonant radius, at $R_{c1} = R_w$. Figure 4 shows the time evolutions of mode amplitudes $d_1 \equiv D_1/R_w$, with halo flux rates controlled by applied voltage asymmetries ϵ_V in addition to $\epsilon_B = 1$. When the halo flux reaches R_{c1} (at times $t_* = 15 \rightarrow 50$ sec), there is immediate damping of the wave amplitude, as

$$d_1(t) = d_1(t_*) - \gamma_1(t - t_*), \quad (2)$$

with γ_1 increasing with increasing flux.

We characterize the outward flux at the critical radius R_{cm} by a normalized “expansion rate” E_m , defined as

$$E_m = -\frac{\dot{N}_L(R_{cm})}{N_L(R_{cm})} = \frac{\int d\theta \dot{N}_L(R_{cm}, \theta)}{N_L(R_{cm})}, \quad (3)$$

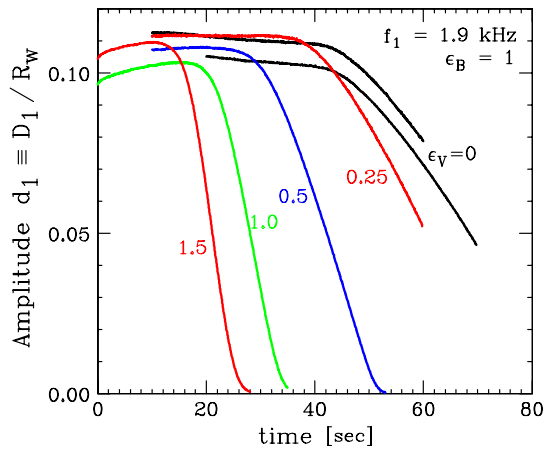


FIG. 4 (color online). Time evolutions of $m = 1$ amplitude $d_1(t)$ with 5 levels of induced flux, showing algebraic damping after the flux reaches $r_1 = R_w$.

where the $\dot{\cdot}$ represents d/dt . The expansion rate E_m is measured with no waves excited, but waves may change the rates somewhat, and the notation $\dot{N}_L(r, \theta)$ includes the possibility of θ -dependent injection of particles into the cat’s eye, as discussed below. We have measured $E_m(\epsilon_B, \epsilon_V)$ for the various applied asymmetries ϵ_B and ϵ_V , both by analyzing halo profiles such as Fig. 2, and by analyzing test wave frequency changes at the 0.1% level. We find that $E_1 \approx E_2$ once the outward flux is fully developed.

Data such as Figs. 3 and 4 then give Fig. 5, showing algebraic damping rates γ_m versus halo expansion rates E_m . For both $m = 1$ and $m = 2$, the algebraic damping is proportional to the number of particles reaching the critical radius. The dashed lines in Fig. 5 show

$$\begin{aligned} \gamma_1 &= (1.5 \pm 0.3)E_1, \\ \gamma_2 &= (3.8 \pm 1.5)E_2. \end{aligned} \quad (4)$$

Here, the stated error bars reflect both shot-to-shot variations and systematic uncertainties (most visible in γ_2) in calculating E , which may itself be modified by wave asymmetries.

We now sketch an analytic model under development, which agrees qualitatively with the observed t^1 (algebraic) damping for $m = 1$, but suggests a possibly discrepant time scaling for $m = 2$. The model posits a θ -uniform outward particle flux superimposed on the wave dynamics, with particles entering the inner edge of the cat’s eye, and then being swept around and outward by the wave, as sketched in Fig. 6. This increase in particle angular momentum is balanced by a decrease in wave angular momentum, i.e., damping of the wave.

For $m = 1$, displacing the column off axis by $-D_1\hat{y}$ results in a cat’s eye potential structure just inside the wall. The wave-frame $\Phi = 0$ contour is inside the wall a distance ρ , with $\rho = 2D_1 \sin(\theta)$ for $0 < \theta < \pi$, and $\rho \approx 0$ for

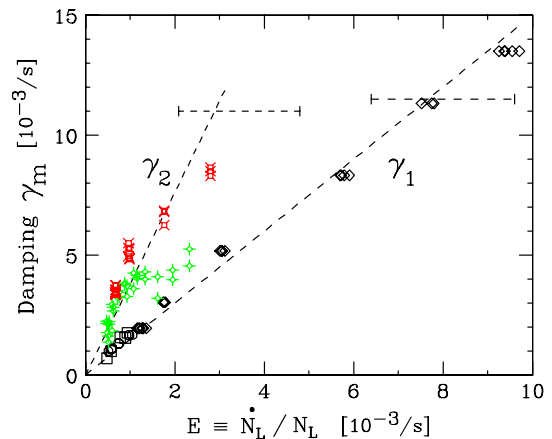


FIG. 5 (color online). Algebraic damping rates γ_1 and γ_2 versus halo flux rate E , from evolutions as in Figs. 3 and 4.

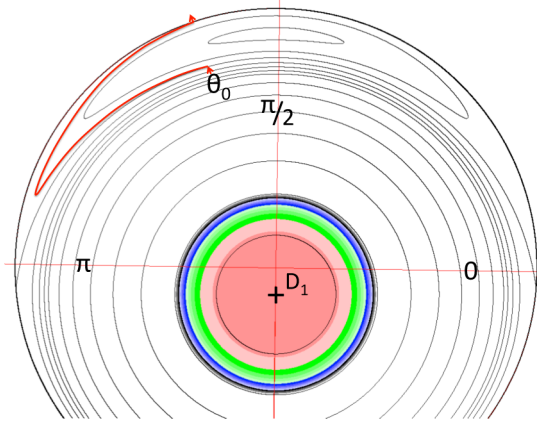


FIG. 6 (color online). Wave-frame potential contours for $m = 1$ mode, with particle trajectory from outward mobility superimposed on wave dynamics.

$\pi < \theta < 2\pi$. With *uniform* outward flow superimposed on the wave-frame dynamics, a particle that enters the cat's eye at some angle θ_0 is swept around to larger θ and back to θ_0 , then exits at the same θ_0 , having gained angular momentum. The particle angular momentum (divided by $eB/2c$) is merely r^2 , so the single-particle change is $\Delta P_1 = 2r\delta r = 2R_w 2D_1 \sin(\theta_0)$, and the total rate of particle angular momentum change is $\dot{P}_N = 4R_w D_1 \int d\theta_0 \dot{N}_L(R_w, \theta_0) \sin(\theta_0)$, where the θ integral is over the cat's eye region of $0 < \theta_0 < \pi$ only. This causes an equal but opposite change in the normalized wave angular momentum, $\dot{P}_w = d/dt(N_L D_1^2) \approx N_L 2D_1 \dot{D}_1$. Equating the particle and wave momenta gives

$$\gamma_1^{(\text{th})} \equiv \dot{d}_1 \equiv \frac{\dot{D}_1}{R_w} = \left(\frac{2}{\pi}\right) E_1, \quad (5)$$

integrating to Eq. (2). Alternately, the same damping rate has been obtained from a more mechanistic analysis, wherein the electric field of the (θ -dependent) scrape-off layer causes a radial $E \times B$ drift of the main plasma, damping the mode.

For $m = 2$, the cat's eye is centered at $R_{c2} \approx \sqrt{2}R_p$, and has a full width around R_{c2} varying as $\rho = 2\sqrt{D_2 R_p} |\sin(\theta)|$. Particles swept outward by the cat's eye then gain momentum as $\dot{P}_N = 4\sqrt{2}R_p \sqrt{D_2 R_p} \times \int d\theta_0 \dot{N}_L(R_{c2}, \theta_0) |\sin \theta_0|$. The normalized wave angular momentum is $N_L D_2^2$, so equating wave and particle momentum gives

$$\gamma_2^{(\text{th})} \equiv \dot{d}_2 \equiv \frac{\dot{D}_2}{R_p} = \left(\frac{4\sqrt{2}}{\pi}\right) d_2^{-1/2} E_2, \quad (6)$$

which integrates to

$$d_2(t) = \left[d_{2i}^{3/2} - \frac{3}{2} \left(\frac{4\sqrt{2}}{\pi} \right) E_2 t \right]^{2/3}. \quad (7)$$

For γ_1 , the measured damping [Eq. (4)] is about twice as large as the model estimate of Eq. (5). This suggests that the outward flux $\dot{N}_L(R_w, \theta)$ *preferentially* enters the $0 < \theta < \pi$ cat's eye, rather than entering the wall at $\pi < \theta < 2\pi$. This is plausible, since idealized $E \times B$ drift velocities are always parallel to the wall.

For γ_2 , the measured damping is about half as large as the Eq. (6) estimate for initial d_2 magnitudes, and no time signature of the $2/3$ exponent is seen experimentally. Both effects suggest that the simple model needs to incorporate the outward radial velocity v_c of the inner cat's eye edge during damping. Damping causes the width ρ to decrease, so the inner edge moves outward towards R_{c2} at velocity $v_c = \dot{\rho}/2$. For Fig. 3 with $\gamma_2 \sim 7 \times 10^{-3}/\text{s}$ at $t \gtrsim t_*$, we estimate $v_c \sim 0.2$ mm/s, which *equals* the halo velocity v_h . Thus, a factor-of-two reduction in γ_2 could easily result, and the “accelerated” $d_2^{-1/2}$ damping prediction of Eq. (6) at small d_2 would be mitigated. Of course, the relative magnitudes of n_h and v_h at any given flux $n_h v_h$ depend on the specifics of the nonideal flux-inducing process. In simulations, we also find that plasma diffusion can affect the late-time evolution.

We note that this flux-induced damping proceeds algebraically as $-\gamma t$ only if the flux is constant in time. That is, Eq. (5) could also be written $\delta D_1 = (2R_w/\pi N_L) \delta N_L$, with no rates at all; in this sense, the damping is analogous to the more visible “spiral arm” damping [13] which results when *large amplitude* $m = 2$ excitation causes the major axis of the ellipse to “inject” particles into the trapping region. In both cases, the damping results from the backreaction as the wave moves particles (vorticity) across the nonlinear trapping region.

This flux-induced damping may be dominant in non-neutral plasmas with nonzero expansion rates [10], and may be important in techniques where precision diocotron mode control is required [5,12]. Moreover, the plasma effects of mobility, diffusion, and viscosity have analogues in nonideal fluid flow. Fluid viscosity causes diffusion of vorticity, and so causes rapid spreading of sharp vorticity edges, and 3D end effects and geostrophic effects may cause outward vorticity fluxes. Thus, this novel flux-driven form of resonant damping may be broadly relevant to both plasmas and geophysical fluids.

This work was supported by NSF and DOE Grants No. PHY0903877, No. PHY0613740, and No. DE-SC0002451.

-
- [1] R. J. Briggs, J. D. Daugherty, and R. H. Levy, *Phys. Fluids* **13**, 421 (1970).
 [2] C. F. Driscoll and K. S. Fine, *Phys. Fluids B* **2**, 1359 (1990).
 [3] K. S. Fine and C. F. Driscoll, *Phys. Plasmas* **5**, 601 (1998).

- [4] J. Fajans, E. P. Gilson, and L. Friedland, *Phys. Rev. Lett.* **82**, 4444 (1999).
- [5] J. R. Danielson, T. R. Weber, and C. M. Surko, *Phys. Plasmas* **13**, 123502 (2006).
- [6] N. S. Pillai and R. W. Gould, *Phys. Rev. Lett.* **73**, 2849 (1994).
- [7] N. Mattor, B. T. Chang, and T. B. Mitchell, *Phys. Rev. Lett.* **96**, 045003 (2006); *Astrophys. J.* **472**, 532 (1996).
- [8] W. D. White, J. H. Malmberg, and C. F. Driscoll, *Phys. Rev. Lett.* **49**, 1822 (1982).
- [9] B. P. Cluggish, C. F. Driscoll, K. Avinash, and J. A. Helffrich, *Phys. Plasmas* **4**, 2062 (1997).
- [10] G. Maero, B. Paroli, R. Pozzoli, and M. Rome, *Phys. Plasmas* **18**, 032101 (2011).
- [11] J. P. Marler and M. R. Stoneking, *Phys. Rev. Lett.* **100**, 155001 (2008).
- [12] C. Canali, C. Carraro, D. Krasnicky, V. Lagomarsino, L. Di Noto, G. Testera, and S. Zavatarelli, *Eur. Phys. J. D* **65**, 499 (2011).
- [13] D. A. Schecter, D. H. E. Dubin, A. C. Cass, C. F. Driscoll, I. M. Lansky, and T. M. O'Neil, *Phys. Fluids* **12**, 2397 (2000).
- [14] N. J. Balmforth, S. G. Llewellyn Smith, and W. R. Young, *J. Fluid Mech.* **426**, 95 (2001).
- [15] R. L. Spencer and S. N. Rasband, *Phys. Plasmas* **4**, 53 (1997).
- [16] V. V. Mikhailenko, H. J. Lee, V. S. Mikhailenko, and N. A. Azarenkov, *Phys. Plasmas* **20**, 042101 (2013).
- [17] L. Landau, *J. Phys. (Moscow)* **10**, 25 (1946).
- [18] D. A. Schecter, *J. Atmos. Sci.* **65**, 2498 (2008).
- [19] R. K. Smith, M. T. Montgomery, and G. L. Thomsen, *Q. J. R. Metrol. Soc.* (2013).
- [20] J. H. Yu, T. M. O'Neil, and C. F. Driscoll, *Phys. Rev. Lett.* **94**, 025005 (2005).
- [21] C. Mouhot and C. Villani, *J. Math. Phys. (N.Y.)* **51**, 015204 (2010).
- [22] Z. Kizner, R. Khvoles, and J. C. McWilliams, *Phys. Fluids* **19**, 016603 (2007).
- [23] Y. A. Tsidulko, T. J. Hilsabeck, and T. M. O'Neil, *Phys. Plasmas* **18**, 084505 (2011).
- [24] M. R. Turner and A. D. Gilbert, *J. Fluid Mech.* **630**, 155 (2009).
- [25] J. M. Kriesel and C. F. Driscoll, *Phys. Rev. Lett.* **87**, 135003 (2001).